Scalable, Versatile Synthesis of Ultrathin Polyetherimide Films and Coatings via Interfacial Polymerization

ADVANCED FUNCTIONAL MATERIALS
www.afm-journal.de

Scalable, Versatile Synthesis of Ultrathin Polyetherimide Films and Coatings via Interfacial Polymerization

Cécile A. C. Chazot, Carl J. Thrasher, Alexander Peraire-Bueno, Michael N. Durso, Robert J. Macfarlane, and A. John Hart**

Polyetherimides (PEI) are high-performance thermoplastic polymers featuring a high dielectric constant and excellent thermal stability. In particular, PEI thin films are of increasing interest for use in solid-state capacitors and membranes, yet the cost and thickness are limited by conventional synthesis and thermal drawing techniques. Here, a method of synthesizing ultrathin PEI films and coatings is introduced based on interfacial polymerization (IP) of poly(amic acid), followed by thermal imidization. Control of transport, reaction, and precipitation kinetics enables tailoring of PEI film morphology from a nanometer-scale smooth film to a porous micrometer-scale layer of polymer microparticles. At short reaction times (≈1 min) freestanding films are formed with ≈1 µm thickness, which to our knowledge surpass commercial state-of-the-art films (3–5 µm minimum thickness) made by thermal drawing. PEI films synthesized via the IP route have thermal and optical properties on par with conventional PEI. The use of the final PEI is demonstrated in structurally colored films, dielectric layers in capacitors, and show that the IP route can form nanometer-scale coatings on carbon nanotubes. The rapid film formation rate and fine property control are attractive for scale-up, and established methods for roll-to-roll processing can be applied in future work.

1. Introduction

Polyetherimides (PEI) are a category of high-performance thermoplastic polymers that combines processability, high strength, excellent thermo-oxidative stability, and flame retardancy.[1–3] Due to this unique combination of properties, PEI materials have been used in a wide range of applications including pharmaceutical process equipment, aircraft interior components,[4] and filtration membranes.[5–8] Since their introduction in 1982,[1] when General Electric commercialized the first PEI under the trade name Ultem, PEI synthesis has relied on time-consuming processes such as solution polymerization of poly(amic acid) (PAA) in a high boiling point solvent, followed by thermal or chemical imidization.[9] Moreover, to shift the reaction equilibrium to the amic acid side, the preparation of PAA requires reflux in dipolar aprotic solvents such as dimethylsulfoxide (DMSO), dimethylacetamide (DMAc), dimethyl formamide (DMF), or N-methyl pyrrolidone (NMP) that can form strong hydrogen–bonded complexes with the carboxyl group.[10] While the reaction rate is generally faster in more common solvents, the main polymerization is often accompanied by a greater number of minor side reactions (e.g., diamine salt formation). These side reactions can negatively affect the purity and molecular weight of the final polymer.

In particular, PEI thin films are used commercially in dielectric capacitors, and significant research and development has focused on scaling melt extrusion techniques down to film thicknesses of 3–5 µm while maintaining low overall cost.[11] Capacitors with thinner films are desirable for use in power electronics for charging of electric vehicles, and PEI is attractive due to its stability at the necessary operating temperatures.[12–14] Moreover, for prospective use in applications such as gas separation,[15–17] structural composites,[18,19] or microelectronics,[20,21] PEI is often further processed to form nanofibers and other nanostructures through methods such as electrospinning,[19] hot-embossing[22] or phase-inversion.[23] These methods rely either on first dissolving PEI in a relevant solvent or on high-temperature drawing, both of which tend to be time and energy intensive because the polymer is particularly resistant to organic solvents and thermally stable. Because of its processing complexity, PEI is more expensive (≈US$28-33 for 25 kg) than other high-performance thermoplastics such as Nylon 6,6 (≈US$2-4 for 25 kg).[24]

Many other high-performance polymers, such as polyamides and polyimides, are commonly processed through interfacial polymerization (IP).[25] IP is a scalable method for manufacturing nanoscale films, fibers, or particles.[26–29] IP combines

C. A. C. Chazot, C. J. Thrasher, A. Peraire-Bueno, M. N. Durso, A. J. Hart
Department of Mechanical Engineering
Massachusetts Institute of Technology
77 Massachusetts Avenue, Cambridge, MA 02139, USA
E-mail: cchazot@northwestern.edu; ajhart@mit.edu

C. A. C. Chazot, C. J. Thrasher, M. N. Durso, R. J. Macfarlane
Department of Materials Science and Engineering
Massachusetts Institute of Technology
77 Massachusetts Avenue, Cambridge, MA 02139, USA

The ORCID identification number(s) for the author(s) of this article can be found under https://doi.org/10.1002/adfm.202214566.

DOI: 10.1002/adfm.202214566

step-growth polymerization with polymer precipitation to control the morphology and final properties of the synthesized materials. For example, IP has been implemented industrially for the formation of thin-film composite membranes for desalination.[30]

In its most common implementation, IP relies on the reaction of an aqueous diamine monomer with an organic bifunctional acid chloride to form a polyamide. Although polyamides have been the main focus of IP due to the rapid rate at which primary diamines react with acid chlorides, the same reaction scheme can be carried out successfully with reactants for which the rate constants are smaller, such as the dianhydride groups used in the synthesis of PEI.[25] There are two principal requirements for synthesizing a polymer via IP. First, the polymerization reaction must be appreciably faster than all side reactions and diffusion/partition of the monomer species. Second, the polymer should remain in solution and reactive for a sufficient time to attain a high degree of polymerization prior to precipitation. Despite the apparent suitability of IP for PEI synthesis, to our knowledge it has not been implemented, likely due to the challenges of balancing the competing solubility requirements of reactants and polymers. Indeed, while PAA intermediates are highly soluble in numerous conventional IP organic solvents such as chloroform or cyclohexanone, dianhydride monomers are barely soluble in the same organic phases.

Here, we present a scalable and versatile route to synthesize PEI films based on IP. PAA is synthesized via IP of an organic dianhydride and aqueous diamine, and then thermally imidized to yield PEI. Using a mixture of organic solvents, we enable rapid IP and selective precipitation of the PAA in a film. The processing times involved are on par with that of commonly used acid chloride-based IP. PAA film formation by IP is governed by diffusion kinetics along with nucleation, growth and coarsening of PAA colloids. The obtained PAA films feature a smooth thin (200–1000 nm) film supported by microparticles on one side; by adjustment of the synthesis parameters we produce flat films or colloid-supported films with tailored dimensions. Nanostructured PEI films obtained after imidization have a glass transition temperature and optical properties on par with that of commercial Ultem, while exhibiting a slightly lower average molecular weight and a broader chain length distribution. We show that the polymer films are structurally colored through thin-film interference/scattering and retain their morphology upon thermal imidization. Finally, we demonstrate how IP of PEI can be used to coat carbon nanotubes (CNTs), and characterize the dielectric properties of PEI films, toward their use in thin film capacitors.

2. Results and Discussion

2.1. Key Considerations for IP of Poly(Amic Acid) (PAA)

First, we evaluated the suitability of various organic solvents to serve as the organic phase for the IP process. To successfully induce IP of the PAA intermediate, the solvent must satisfy the following criteria (**Figure 1**a): (1) It must be insoluble in water, enabling the formation of a liquid-liquid interface and preventing hydrolysis of the dianhydride; (2) it must dissolve small quantities of the diamine monomer, enabling the partition of the aqueous monomer into the organic solvent and subsequent reaction with the dianhydride at the interface; and (3) it must have both high solubility for the organic monomer and low solubility for the PAA, enabling precipitation of a polymer film at the interface. Additionally, solvents with a low boiling point (<150 °C) are preferable to facilitate polymer purification. We focused on the formation of conventional PAA and subsequent PEI derived from m-phenylene diamine (MPD) and 4,4′- bisphenol A dianhydride (BPADA) monomers (Figure 1b). To choose a suitable organic phase, we considered 20 common organic solvents and evaluated their potential for dissolving PAA and BPADA using Hansen solubility parameters (Table S1 and Figure S2, Supporting Information).[31] We follow Hansen's definition of the dispersive, polar, and hydrogen solubility parameter components such that the total solubility parameter is defined as:

$$\delta_T = \left(\delta_D^2 + \delta_P^2 + \delta_H^2\right)^{1/2} \tag{1}$$

We then represent the interaction between selected solvents and PAA and BPADA graphically (Figure 1c), where $\delta_V = (\delta_D^2 + \delta_P^2)^{1/2}$ and δ_H are plotted on the axes. This 2D representation has been demonstrated to be the most effective way to visualize polymer–solvent interactions.[32] We considered solvents used in conventional PEI synthesis as well as common organic phases in the IP of polyamides. Most of the points representing good solvents for a given solute fall into a circular region centered on the solute coordinates (δ_V, δ_H) with a radius $R_M \approx 5$ MPa$^{1/2}$. The ability of a solvent to dissolve a given solute can determined by the distance between the Hansen solubility parameters of the two species on the plot:[32]

$$\Delta\delta_2 = \sqrt{\left(\delta_{V,2} - \delta_{V,1}\right)^2 + \left(\delta_{H,2} - \delta_{H,1}\right)^2}. \tag{2}$$

To satisfy criterion (3), the (δ_V, δ_H) values for the solvent must lie outside the PAA solubility circle yet remain within the BPADA circle. This means that the distance between the solvent point and PAA (denoted $\Delta\delta_{PAA}$) must be greater than the distance between the solvent and BPADA (denoted $\Delta\delta_{BPDA}$), while remaining within the BPADA solubility circle. We therefore can write the condition: $\Delta\delta_{PAA} - \Delta\delta_{BPDA} > 0$ and $\Delta\delta_{BPDA} < R_M$. Abbreviations and graphical representation including the 20 solvents considered here and various solubility parameter methods can be found in Supporting Information (Figure S2 and Tables S1 and S2, Supporting Information).

In this condition, the most promising organic solvent for IP of PAA was acetophenone (ACP) with $\Delta\delta_{PAA} - \Delta\delta_{BPDA}$ = 1.8 MPa$^{1/2}$ and $\Delta\delta_{BPDA}$ = 2.84 MPa$^{1/2}$. However, we found experimentally that ACP dissolves PAA, preventing polymer film precipitation in IP. We therefore considered hydrophobic mixtures of solvents and calculated their Hansen solubility parameter components as a function of the volume fraction of solvent B in solvent A:

$$\delta_{i,\mathrm{AB}} = \left(1 - \phi_B\right)\delta_{i,A} + \phi_B\delta_{i,B} \tag{3}$$

where ϕ_B is the volume fraction of solvent B in the mixture, and the subscript $i = D$, P, *or* H for the dispersive, polar, and

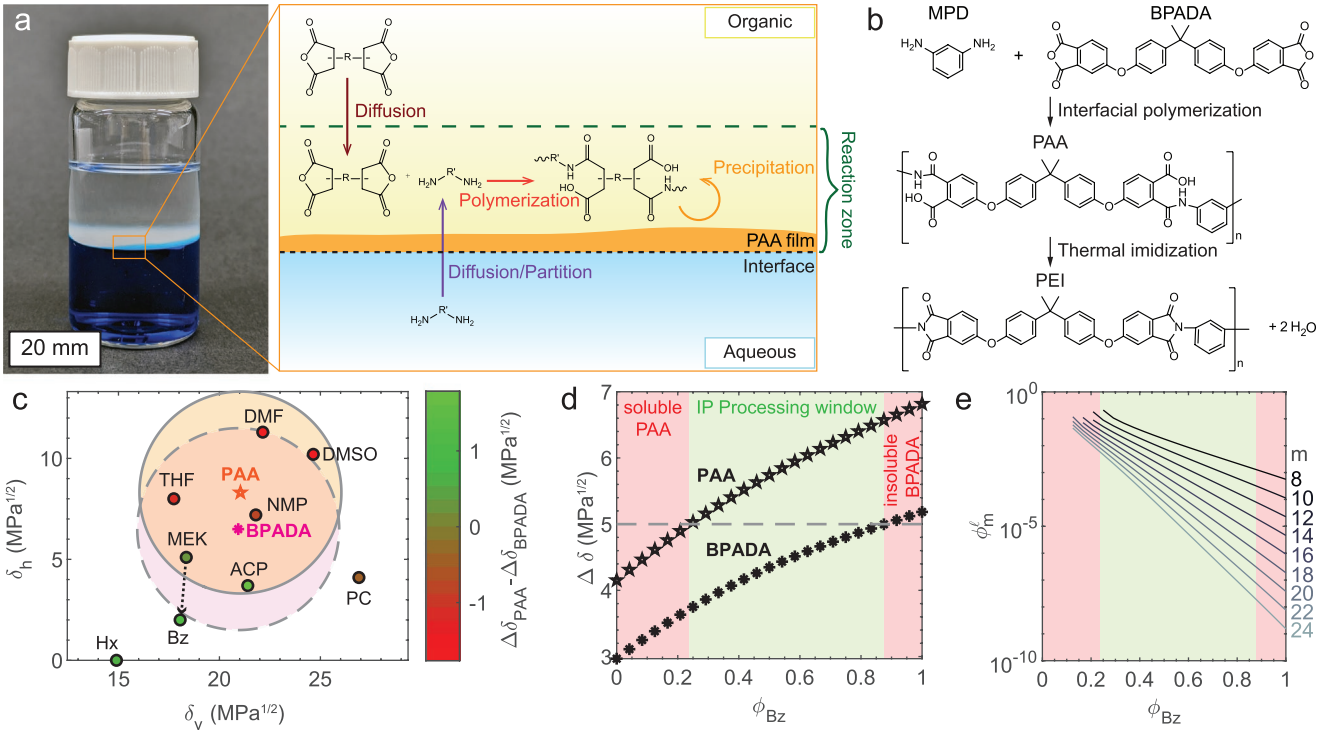

Figure 1. IP of poly(amic acid) (PAA). a) Photograph of IP with aqueous diamine and organic dianhydride, and schematic describing the various transport and reaction kinetics involved. b) Reaction scheme involving aqueous m-phenylene diamine (MPD) and organic bisphenol A dianhydride (BPADA), which have been chosen here for the formation of thermoformable BPADA-MPD polyetherimide (PEI). c) Solubility of PAA in various solvents in the $\delta_v - \delta_h$ diagram. Solvents selected are methyl ethyl ketone (MEK), benzene (Bz) and mixtures thereof. Increasing the Bz fraction in MEK induces an evolution of solubility parameter indicated by the dashed arrow. d) Solubility parameter distance between MEK-Bz mixtures and PAA and BPADA respectively as a function of benzene volume fraction. e) Limit of solubility (reported as the corresponding volume fraction of PAA chains of length m for the lower binodal branch) as a function of the volume fraction of Bz in the solvent mixture. The regions marked in red correspond to the predicted volume fraction of Bz from Hansen solubility parameter calculation.

hydrogen components, respectively. The coordinates of the A–B solvent mixture ($\delta_{V,mix}$, $\delta_{H,mix}$) for various solvent ratios can be represented graphically as situated on a straight line joining ($\delta_{V,A}$, $\delta_{H,A}$) and ($\delta_{V,B}$, $\delta_{H,B}$). With this in mind, we considered mixtures of a solvent for both PAA and BPADA (methyl ethyl ketone (MEK)), with an organic phase that sparingly dissolves BPADA and is an antisolvent for PAA (benzene (Bz)). By plotting $\Delta\delta_{PAA}$ and $\Delta\delta_{BPDA}$ as a function of the fraction of Bz in MEK, it is possible to evaluate optimal solvent ratios for IP of PAA (Figure 1d). We found that mixtures of MEK:Bz with $0.24 \leqslant \phi_{Bz} \leqslant 0.87$ was a good solvent for the monomer and a non-solvent for the polymer, making it a suitable organic phase for implementing IP of PAA.

Using Flory–Huggins theory,[33] we can also predict the limit of solubility for PAA polymer chains of various lengths from the intersection of the lower binodal branch with the horizontal line corresponding to the value of the polymer-solvent interaction parameter. The limit of solubility ϕ_m^ℓ is found to decay exponentially with benzene volume fraction in the organic phase (Figure 1e). The magnitude of decay depends on m, the number of repeat units in the polymer chain. We found that:

$$\phi_m^\ell \propto e^{-m\phi_{Bz}} \quad (4)$$

We predicted that precipitation of polymer chains containing ⩾8 repeat units is induced at $\phi_{Bz} \geqslant 0.27$, while increasing benzene content during IP would result in earlier polymer film precipitation and lower overall molecular weight.

2.2. Morphology of PAA Films Synthesized by IP

As in the case of conventional IP,[25] we found that PAA films formed by IP of BPADA with MPD formed on the organic side of the interface. However, unlike in conventional IP, where the film shows stripe-like Turing nanostructure,[28] IP-PAA films were found to have a multiscale morphology comprising (1) a smooth, thin (≈100 nm) film that forms closest to the liquid-liquid interface, and (2) a layer of spherical colloids with diameters $d_c \approx 1$ µm that forms on the side of the film corresponding to the organic phase. Investigation of film morphology versus reaction time t_{rxn} indicated that PAA precipitation in IP is governed by the kinetics of nucleation, growth, and coarsening (**Figure 2**). In the incubation phase corresponding to short reaction times, there is no PAA precipitation (Figure 2a-I). Although the concentration of polymer chains increases, it remains below its limit of solubility or critical super-saturation to induce phase separation. Once the critical supersaturation is reached, the flat, thin film of PAA precipitates in the immediate vicinity

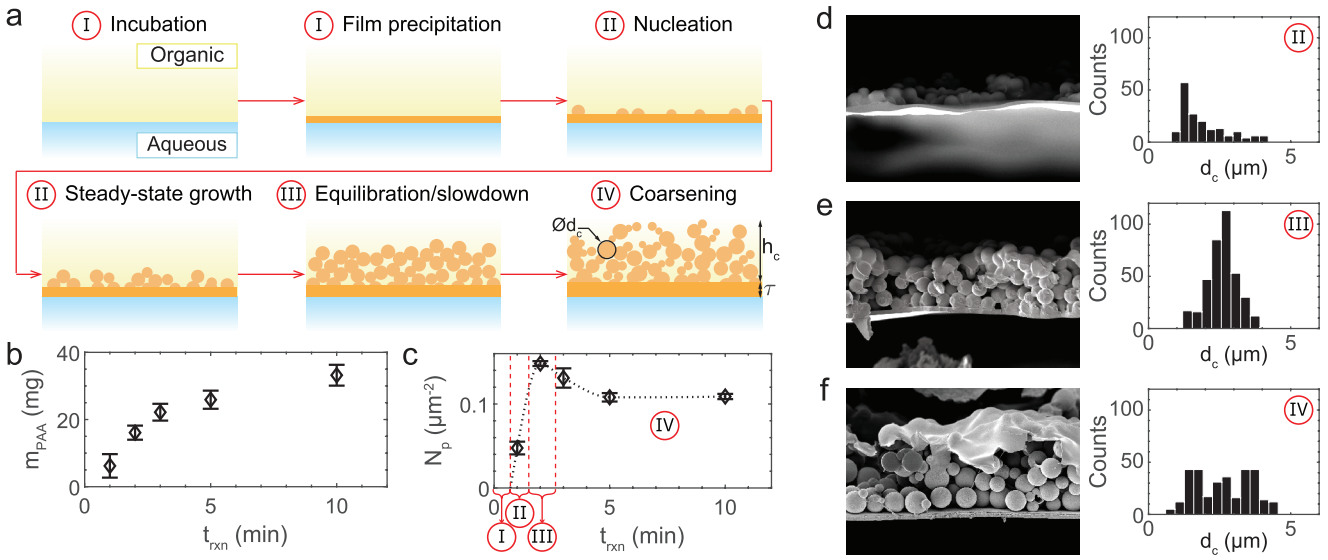

Figure 2. Nucleation-growth-coarsening governs the morphology of PAA films produced by IP. a) Schematic showing the evolution of PAA film morphology as reaction time increases. b) Evolution of the mass of the PAA film with reaction time. (c) Evolution of the areal concentration of colloids with reaction time showing the four stages of the nucleation-growth-coarsening mechanism. d–f) SEM images showing the cross-section of PAA films, with corresponding colloid diameter distribution and associated stage (II-IV) indicated. All data were obtained for a monomer concentration $[MPD] = [BPADA] = 0.07$ mol L^{-1} and $\phi_{Bz} = 0.3$ to maximize the yield of reaction.

of the liquid-liquid interface. This flat film supports steady-state nucleation and growth of polymer colloids (Figure 2a-II) until the concentration of PAA in the solid state approaches its equilibrium value and growth slows (Figure 2a-III). Longer reaction times cause coarsening of the colloids, broadening of their size distribution, and a decrease in number density (Figure 2a-IV).

This evolution was confirmed experimentally by examining the temporal evolution of the mass of the polymer film m_{PAA}, the areal number concentration of colloids N_p, and the PAA film morphology (Figure 2b–f). We found that PAA precipitation did not occur at reaction times below 30 s, and that the yield of reaction increased quickly before slowing down for $t_{rxn} \geqslant 3$ min (Figure 2b). The measured evolution of N_p with reaction time is typical of a nucleation-growth-coarsening mechanism, showing the characteristic stages of the governing kinetics (Figure 2c).[34,35]. We found that steady-state nucleation and growth of polymer colloids occurred for $t_{rxn} \leqslant 2$ min, while coarsening happened for $t_{rxn} \geqslant 3$ min. Characteristic SEM images of the cross-sectional morphology of PAA films obtained in various phases of the nucleation-growth-coarsening process are shown in Figure 2d–f. While growth initially results in more colloids with a relatively tight diameter distribution d_c, increasing the reaction time causes the colloid size distribution to broaden. This suggests a coarsening effect with larger particles growing and smaller particles shrinking.

In conventional IP with diamines and acid chlorides, polymer film formation primarily occurs by spinodal decomposition.[36,37]. Here, the precipitation of PAA in IP is driven by nucleation because of the slower polymerization kinetics for dianhydride-based reactions than for acid chloride-based interfacial polycondensations. Nucleation has been observed to occur at long timescales in conventional IP after monomer depletion,[37] or in IP reactions featuring slow polymerization kinetics such as oxidative polymerization of polyaniline.[38] Indeed, step-growth polyaddition of PAA from BPADA and MPD results in rate constants of $\approx 10^0 - 10^2$ L mol^{-1} s^{-1},[39] between that of IP of polyamides ($\approx 10^2 - 10^5$ L mol^{-1} s^{-1})[25] and polyaniline ($\approx 10^{-3} - 10^0$ L mol^{-1} s^{-1}).[40] From this we conclude that IP of PAA enables the same nanoscale control of polymer morphology as in oxidative IP with processing times comparable to those of interfacial polycondensation of polyamides.

2.3. Kinetics of PAA Film Formation by IP

Having identified that PAA film formation is governed by nucleation, growth, and coarsening, we studied the influence of the polymer solubility limit and polymerization reaction rate on film morphology (**Figure 3**). The morphology of the PAA films can be described by the thickness of the flat film τ, the average colloid diameter d_c, and the height of the colloid layer h_c. Increasing benzene content ϕ_{Bz} in the organic phase, and therefore decreasing the solubility of PAA ϕ_m^ℓ (Figure 4) results in a decrease of τ and d_c (Figure 3a). At very high benzene volume fractions (ϕBz $\geqslant 0.7$), the colloids were found to coalesce near the top of the layer, farthest from the interface. We studied the influence of polymerization rate by varying the initial monomer concentration $[BPADA]_0 = [MPD]_0 = [M]_0$ at a fixed benzene ratio ($\phi_{Bz} = 0.3$) and reaction time ($t_{rxn} = 5$ min) (Figure 3b). When the concentration of monomer was low (and therefore polymerization was slow), a thin PAA film with no colloids formed. Increasing the monomer concentration resulted in an overall thickening of the flat film and of the colloid layer.

Observing the dependence of τ, d_c, and h_c on synthesis parameters sheds light on the interplay of transport, reaction, and precipitation kinetics in IP of MPD with BPADA (**Figure 4**). We first focused on the influence of the PAA solubility limit and ϕ_{Bz}, to compare the processing window and power-law dependence with

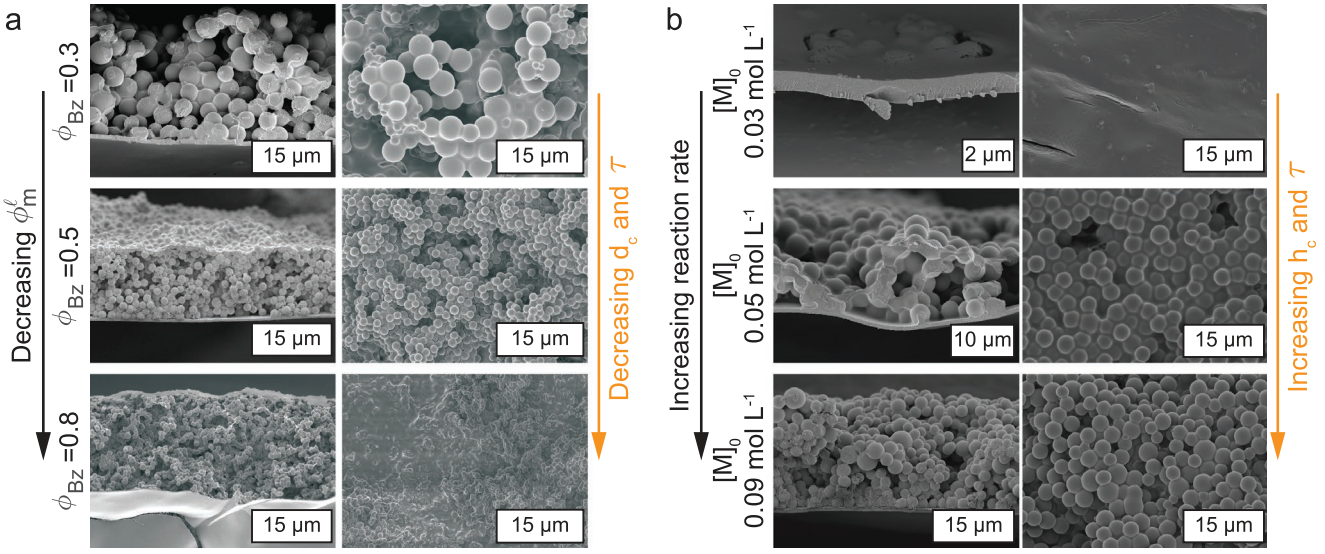

Figure 3. The dependency of film morphology on IP kinetics. a,b) SEM images of the cross-section of the polymer film and the top surface facing the organic side of the interface when adjusting (a) the PAA solubility limit in the organic phase or (b) the rate of polymerization reaction. All data were obtained for a reaction time of 5 min. The influence of ϕ_{Bz} was studied at constant $[MPD]_0 = [BPADA]_0 = 0.07$mol L^{-1}. The influence of monomer concentration was studied at constant $\phi_{Bz} = 0.3$.

predictions derived from Hansen solubility parameters and Flory-Huggins theory (Figure 4a–c). For a benzene content of $\phi_{Bz} \leqslant 0.2$, no PAA film was formed at the liquid-liquid interface. Similarly, for $\phi_{Bz} \geqslant 0.9$, BPADA cannot be fully dissolved at a concentration of $[BPADA]_0 = 0.07$ mol L^{-1} in the organic phase. Both these findings are consistent with Hansen solubility parameter predictions. Within the IP processing window of benzene content, we found that both τ (Figure 4a) and d_c (Figure 4b) decreased exponentially with ϕ_{Bz}, with two different exponential constants, while h_c remained independent of the PAA solubility limit. The exponential dependence of these two characteristic sizes can be understood from nucleation kinetics, providing further evidence that it is the governing precipitation mechanism. Indeed, Twomey theory for supersaturation nucleation predicts that the number concentration of the critical nuclei (CN), represented by N_{CN}, is related to the supersaturation S by a power law:[41,42]

$$N_{\mathrm{CN}} = \frac{n_{\mathrm{CN}}}{V} \propto S^k \tag{5}$$

where k typically varies from 0.2 to 0.5, n_{CN} is the number of CN and V is the total volume considered for nucleation. Adapting this to the precipitation of PAA spherical particles for a total precipitated volume $V_{\mathrm{CN,tot}} = n_{\mathrm{CN}} \frac{4\pi(d_{\mathrm{CN}}/2)^3}{3}$, where d_{CN} is the diameter of a CN, we find that:

$$d_{\mathrm{CN}} \propto S^{-\frac{k}{3}} \tag{6}$$

This can be rewritten for each polymer chain length m as follows:

$$d_{\mathrm{CN},m} \propto S_m^{-\frac{k}{3}} \tag{7}$$

We know the supersaturation of polymer chains of size m in the organic solution is obtained from the volume fraction of polymer chains of size m in the control volume ϕ_m according to:

$$S_m = \frac{\phi_m - \phi_m^\ell}{\phi_m^\ell} \propto \frac{1}{\phi_m^\ell} \tag{8}$$

Considering ϕ_m^ℓ dependence on ϕ_{Bz} based on Flory–Huggins theory described by Figure 4, we find that:

$$d_{\mathrm{CN},m} \propto e^{-\frac{mk}{3}\phi_{Bz}} \tag{9}$$

This corresponds to the exponential dependence observed experimentally, enabling us predict the approximate molecular weight of PAA by considering k values in the typical 0.2–0.5 range. Based on the evolution of spherical colloid diameter d_c with ϕ_{Bz}, we find that PAA synthesized by IP is expected to have an m of 12 to 20 repeat units, a chain length on par with that of conventional IP of aromatic polymers.[43] The choice of d_c over flat film thickness τ is justified by the fact that the Twomey theory assumes that the CN are of spherical geometry.

Observing the dependence of τ, d_c, and h_c on reaction time provides further information on the kinetics of IP based on a dianhydride (Figure 4d,e). Both τ and h_c exhibit a square-root dependence on reaction time. This indicates that IP of BPADA with MPD is a diffusion-limited process, similar to its conventional counterpart using diamine and acid chloride monomers.[36,37]. The average colloid diameter d_c, however, does not follow a square-root evolution with t_{rxn}, due to particle coarsening. The broadening of the colloid size distribution results in a larger standard deviation and an ill-defined average d_c value.

Last, we quantified the influence of the polymerization reaction rate on film thickness by varying the concentration of the monomer (Figure 4g–i). We found that the thickness of the thin polymer layer τ increased with monomer concentration for $[M]_0 \leqslant 0.07$ mol L^{-1} before plateauing at high $[M]_0$ (Figure 4g),

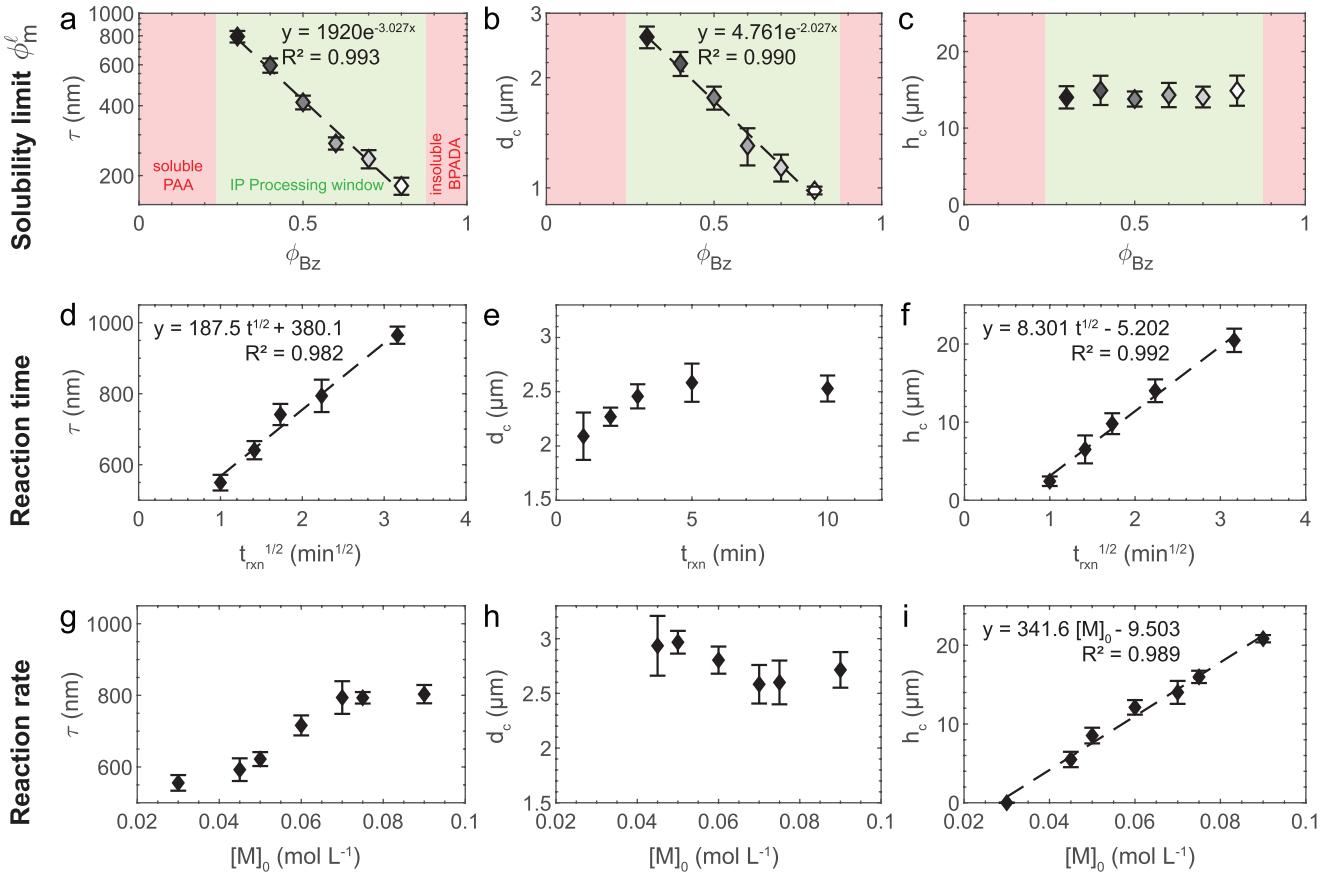

Figure 4. Interplay of transport, reaction, and precipitation kinetics in IP of PAA. a–c) The IP processing window and PAA morphology evolution with decreasing polymer solubility. The regions marked in red were verified experimentally: no polymer film formed for $\phi_{Bz} \leqslant 0.2$, and BPADA could not dissolve for $\phi_{Bz} \geqslant 0.9$; the same regions are indicated in Figure 1. Exponential dependence of τ and d_c with ϕ_{Bz} demonstrate that precipitation occurs by PAA nucleation. All data were obtained for a monomer concentration $[MPD]_0 = [BPADA]_0 = 0.07$ mol L^{-1} and $t_{rxn} = 5$ min. d–f) Influence of reaction time on PAA film morphology and corresponding square-root dependence of τ and h_c showing that IP of PAA is a diffusion-limited process. All data were obtained for a monomer concentration $[MPD]_0 = [BPADA]_0 = 0.07$ mol L^{-1} and $\phi_{Bz} = 0.3$. g–i) Influence of polymerization reaction rate on PAA film morphology. The linear dependence of h_c with monomer concentration indicates that IP of MPD with BPADA is a pseudo-first order reaction. All data were obtained for $t_{rxn} = 5$ min and $\phi_{Bz} = 0.3$.

while d_c showed no dependence on reaction rate (Figure 4h). Only h_c exhibited a clear linear dependence on monomer concentration (Figure 4i). This observation is consistent with observations from IP of polyamide based on acid chloride monomers.[44,45] At low monomer concentrations, and at the onset of diamine partitioning (where the reaction takes place in the immediate vicinity of the interface), the reaction is controlled purely by the diffusion of the diamine into the organic phase. The reaction occurs instantaneously and the film thickness is $\propto [M]_0^k$, with k between 1.5 and 2.[44,45] As the concentration of organic monomer increases, the asymptotic limit $\frac{[\mathrm{BPADA}]_0}{[\mathrm{MPD}]_r} \to \infty$ is reached, with $[MPD]_r$ being the concentration of MPD that diffused and partitioned into the reaction zone on the organic side of the interface. This results in a pseudo-first order reaction in monomer concentration, in which the film thickness increases linearly with $[M]_0$. In the pseudo-first order reaction case, the reaction takes place in a homogeneous manner (on a microscopic scale) in a zone of finite thickness. In the instantaneous reaction case, by contrast, the reaction proceeds in a heterogeneous manner, at an infinite rate in a zone of near zero (nanoscale) thickness.[44] This explanation, derived for IP of acid chloride monomers, can be used to elucidate the evolution of τ and h_c with monomer concentration. As observed from varying t_{rxn}, the flat thin film forms first at the immediate vicinity of the liquid-liquid interface before supporting the nucleation of PAA colloids on the side in contact with the organic phase. This explains the dependence of τ on $[M]_0$. At low monomer concentrations, polymerization proceeds in the instantaneous reaction regime, while at high monomer concentrations the pseudo-first order assumption is more valid. In contrast, PAA colloids only form in later reaction stages, at a distance of 1 – 20 μm from the liquid-liquid interface. The evolution of h_c with $[M]_0$ therefore lies within the pseudo-first order reaction assumption and features a linear dependence.

In general, we found that τ is governed by, in decreasing order of influence, the kinetics of precipitation, diffusion/partition, and reaction rate. However, d_c is exclusively dictated by precipitation of PAA through the thermodynamic solubility limit and kinetics of nucleation, independent of the diffusion-reaction of the monomer species. Finally, h_c is governed by the rates of diffusion and reaction, and is not influenced by the PAA solubility limit in the organic phase. Linking polymer

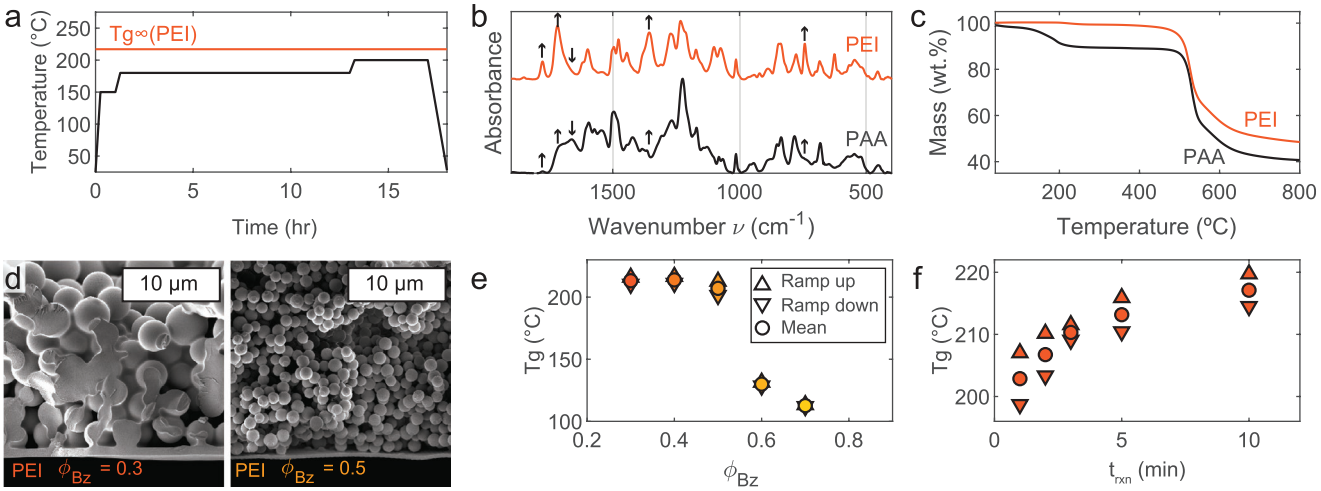

Figure 5. Imidization of PAA to form PEI films. a) Temperature ramp for thermal imidization of PAA to form PEI. b) FTIR spectra of PAA and PEI obtained by thermal imidization. Arrows indicate the vibrational mode peaks that increase (arrow up) or decrease (arrow down) in intensity with imidization. c) Thermal decomposition profile of PAA and PEI demonstrating little to no water loss suggesting complete imidization. d) Assessment of the morphology of PEI films obtained from PAA synthesized by IP at $\phi_{Bz} = 0.3$ and $\phi_{Bz} = 0.5$ showing structure retention upon thermal imidization. e,f) Evolution of T_g with benzene content (e) and reaction time (f) as measured by Differential Scanning Calorimetry (DSC).

morphology to IP reaction parameters elucidates the kinetics governing the reaction and enables process optimization for tailoring of polymer properties.

2.4. Imidization of PAA to form PEI

To form PEI, we performed thermal imidization of the PAA films under vacuum for 1 h at 150 °C, followed by 12 h at 180 °C, then 4 h at 200 °C (**Figure 5**a). We chose the temperature profile to remain below $T_{g,\infty} = 217$ °C, the maximum glass transition temperature that can be achieved at a theoretically infinite molecular weight. Fourier Transform Infrared (FTIR) spectroscopy and Thermogravimetric Analysis (TGA) demonstrate that this heat treatment results in nearly complete imidization (Figure 5b,c). FTIR spectra show an increase in the intensity of peaks that are characteristic of imide ring vibrational modes and a decrease in those corresponding to secondary amide deformation (Figure 5b). Specifically, peaks characteristic of asymmetric (ν = 1776 cm^{-1}) and symmetric (ν = 1716 cm^{-1}) imide cabonyl stretching as well as imide ring C–N stretching (ν = 1350 cm^{-1}) and bending (ν = 740 cm^{-1}) were found to increase in intensity. Further, peaks characteristic of secondary amide deformation (ν = 1661 cm^{-1}) show negligible intensity after imidization, demonstrating a high degree of conversion. Similarly, TGA profiles of PEI indicate no water loss upon heating, demonstrating the extent of imidization (Figure 5c). By SEM imaging, we found that the film morphology is retained upon thermal imidization, with no noticeable shrinkage or colloid sintering (Figure 5d).

One of the main processing advantages of PEI is its thermoformability. With this in mind, we assessed how the glass transition temperature T_g of PEI films obtained by IP evolves in relation to reaction parameters (Figure 5e,f). We found that T_g depends strongly on benzene volume fraction, with a considerable decrease observed for $\phi_{Bz} \geqslant 0.6$ (Figure 5e). This is consistent with the experimental observation that PAA films obtained in these conditions flowed during imidization, losing their micro/nanoscale features. In contrast, we found that T_g gradually increased with increasing reaction time before plateauing at a value of ~215 – 217 °C, which is comparable to T_g of commercially produced Ultem (Figure 5f).[46] T_g was also found to be independent of monomer concentration.

The evolution of T_g properties with IP synthesis parameters can be explained by observing the molecular weight of the obtained PEI films. Using Gel Permeation Chromatography (GPC), we characterized the molecular weight distribution of polymer films obtained in a broad range of IP conditions (Tables S3, S4, and S5, Supporting Information). We focused on the number average molecular weight M_n as the Flory–Fox equation predicts the relationship between M_n and T_g:[47]

$$T_g = T_{g,\infty} - \frac{K}{M_n} \tag{10}$$

where K is an empirical parameter related to the free volume present in the polymer sample. We can therefore observe the dependence of M_n on ϕ_{Bz}, t_{rxn}, and $[M]_0$ (Figure S12, Supporting Information). M_n was found to decrease with benzene volume fraction, as expected from Flory–Huggins theory and the predicted solubility limit (Figure S12a, Supporting Information). Note that M_n ~ 6,000 g mol^{-1} corresponds to ≈10 repeat units, a value close to predictions using Twomey nucleation theory. The polydispersity index (PDI) was found to be between 5 and 6 and somewhat independent of benzene volume fraction. For $\phi_{Bz} \geqslant 0.6$, PEI chains were found to be very short, comprising fewer than 10 repeat units. This supports the drop in T_g observed experimentally under these IP conditions. M_n was also found to increase with reaction time before reaching a plateau for $t_{rxn} \geqslant 5$ min (Figure S12b, Supporting Information), also supporting the observed T_g trend. Moreover, we found that M_n slightly increases with $[M]_0$ from 4,613 g mol^{-1} at 1 min to 8,047 g mol^{-1} after 10 min (Figure S12c). We observed that the

PDI of films with a low number of colloids (t_{rxn} = 1 min and $[M]_0$ = 0.045 mol L^{-1}) is less than that of thicker films with a high concentration of colloids (Tables S4 and S5, Supporting Information). This suggests that the PDI of the thin polymer films is lower than that of the later-formed polymer particles.

The final PEI films show values of M_n slightly lower than that of commercial Ultem (M_n = 12 000 g mol^{-1} for Ultem 1040), and larger values of PDI (PDI = 2.9 for Ultem 1040).[48] The lower value of M_n may result in a PEI with lower tensile strength, elongation at break, or impact strength.[46,49] However, the larger PDI could provide an opportunity to improve processability, as broader molecular weight distributions (PDI ⩾ 4) are often used to decrease shear rate, particularly in injection molding and extrusion processing.[49]

2.5. Functional Properties and Potential Applications of IP-derived PEI

2.5.1. Structural colors

PAA films obtained by IP, as well as their imidized PEI counterparts, exhibit structural colors. Films obtained in different IP conditions appear dim green, blue, yellow, or pink to the naked eye, indicating that the reflection spectrum depends on the film morphology (**Figure 6**a). Benzene content greatly influenced structural color, while reaction time and monomer concentration did not affect the reflection peaks of the films. Structural colors were retained upon imidization in films obtained with a low benzene content (Figure 6b). This observation is consistent with the preserved morphology at high polymer molecular weight. Using Rouard's theory, we found that the reflection peaks in PAA and PEI films arises from thin-film interference with the smooth nanoscale layer, with no contribution of the colloids to the reflection maxima (Figure 6c). Fitting the experimentally measured reflection spectra with Rouard's prediction for a film of thickness τ (as measured by SEM), we found that PAA films feature a refractive index of 1.65, which aligns with reported values for similar PAAs.[50] The refractive index increases to 1.72 following imidization, consistent with published values for PEI and commercial Ultem.[51,52]

While colloids do not affect the reflection maxima, they do influence the spectrum background intensity (Figure 6d). Scattering attenuates the perceived color compared to that predicted using Rouard's method (Figure 6e). More information on the influence of particle size and number on optical scattering and structural colors can be found in Figure S15 (Supporting Information).

2.5.2. Thin-film capacitors

Commercially manufactured PEI films are commonly used as a dielectric layer in thin-film capacitors; these thin sheets are typically made by extrusion of PEI followed by film drawing, and to our knowledge the lower-bound thickness is limited to 3–5 µm.[53] To show the suitability of IP-derived PEI for this application, prototype capacitors were fabricated from films obtained by IP at ϕ_{Bz} = 0.3, and t_{rxn} of 3, 5, and 10 min (**Figure 7**a,b), resulting in various thicknesses. Proper electrical contact between the electrodes and the PEI dielectric layer was ensured using conductive silver paste that conformed to the surface of the colloid layer (Figure 7a).

As expected, the capacitance scaled inversely with film thickness (Figure 7b). The measured values were compared to calculations taking into account the overall film thickness $h_{tot} = \tau + h_c$ and porosity, and assuming a dielectric constant of 2.96 (equal the square of the measured refractive index of 1.72). Much higher capacitance values could be obtained by testing nanometer-scale smooth film without colloids, although their handling remains challenging due to the current fragility of these films and cracking upon solvent evaporation. Another improvement route could be to infiltrate the porous colloid layer with a second material with a high dielectric constant to form a composite thin film capacitor.

2.5.3. Nanocomposites

Last, we show that IP-based PEI synthesis can be translated to create complex nanocomposites, for example by conformally

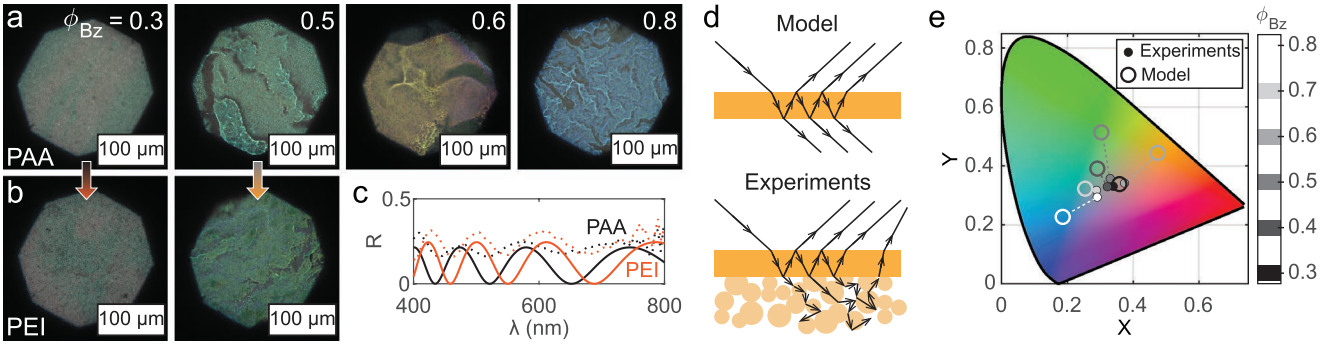

Figure 6. Structural colors in PAA and PEI films from this study. a,b) Top-down views of PAA (a) and PEI (b) films showing structural colors arising from thin-film interference effects. Images were obtained by optical microscopy, with the flat side of the film closest to the objective lens. c) Representative experimental reflection spectra (dotted line) and spectra calculated using Rouard's method and values of τ estimated by SEM (solid line), using a refractive index of 1.65 for PAA and 1.72 for PEI. d) Schematic showing how PAA colloids act as light scatterers, resulting in decreased iridescence of the structural color compared to Rouard's theoretical prediction. e) CIE color plot comparing experimental and model spectra for various benzene volume fractions.

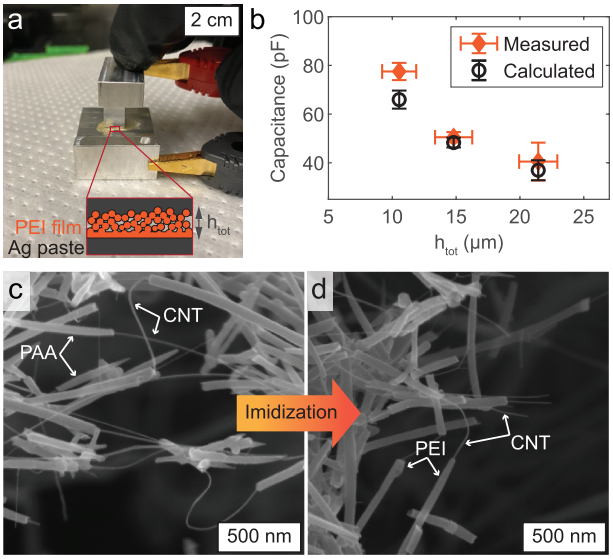

Figure 7. Potential applications of IP of PEI. a) Photograph showing the experimental apparatus for PEI film capacitance measurement. The two aluminum electrodes sandwich a PEI film and are directly connected to a LCR meter. Electrical contact is ensured by applying a conformal coating of silver paste to the colloid layer. b) Measured and calculated capacitance for PEI films of various thicknesses. c) Cross-sectional image of CNT-PAA composites obtained by ISIP. d) Conformal polymer conformal coating is retained upon imidization.

coating CNTs. This was achieved through in-situ interfacial polymerization (ISIP) (Figure 7c,d).[54,55] ISIP results in nanocomposites with a tailored morphology through the interplay of fluid displacement, transport-reaction kinetics, and polymer precipitation. Unlike IP at the static liquid-liquid interface, ISIP relies on the sequential immersion of a porous substrate in the aqueous and organic phase. In ISIP, the CNT sheet is first immersed in the aqueous MPD solution to saturate the pores with the liquid, and then transferred to the organic phase to induce simultaneous fluid displacement, monomer partition, and polymerization. Upon contact with the organic phase, the BPADA solution wicks into the network by capillary action, simultaneously displacing the aqueous phase and reacting with MPD by IP.

PAA synthesized by ISIP formed a conformal coating around individual CNTs (Figure 7c) that retained its morphology upon imidization (Figure 7d). This is explained by the aromatic structure of both PAA and PEI that enables π-interaction with the CNTs, and chain alignment parallel to the CNT outer wall.[55] Further evidence of π-interaction through FT-IR measurement can be found in the Supporting Information.

2.6. Discussion

The differences between traditional IP (e.g., of polyamides) and the use of dianhydride monomers in this work is noteworthy, and implications for potential synthesis scaleup must be considered. Table S6 (Supporting Information) summarizes the similarities and differences between dianhydride-based IP and conventional diacid-chloride-based IP. First, dianhydride monomers are less hazardous and more stable in ambient conditions than the diacid chlorides used in IP of polyamides. Moreover, because only water is released in imidization, the use of dianhydrides also results in a polyaddition IP reaction with no harmful byproducts, unlike traditional IP that releases hydrochloric acid upon polymerization. Although the lower reactivity of dianhydride results in smaller reaction rate constants and longer processing times, films are formed at rates ≈1 μm min^{-1}.

In this work, imidization of PAA to PEI is the most time-consuming step, and must be performed below the polymer T_g to retain the film morphology. Employing chemical imidization or conducting IP at a higher temperature with less volatile solvents could circumvent this challenge and significantly reduce processing times. Importantly, IP of PEI offers finer control over polymer film morphology than conventional IP due to the nucleation-growth-coarsening precipitation mechanism.

Moreover, while the thermal and optical properties of PEI obtained by IP are on par with those of commercial Ultem, its molecular weight remains slightly lower and its PDI greater. This outcome could be improved by using another suitable solvent mixture such as dichloromethane with chlorobenzene (Figure 1 and Table S1, Supporting Information) or by increasing diffusion/partition of the diamine in the organic phase using a phase-transfer agent, as in IP of polyamides.[56]

For industrial scale-up, IP-based processing of PEI could be implemented in a roll-to-roll manner. This would enable fine control of reaction times and film thickness, as has been shown with manufacturing of polyamides used in thin-film composite membranes.[57] Film handling could be improved by process automation along with careful tension control. Moreover, for ultrathin films the use of a carrier substrate may be necessary, and is well-known practice for current industrial-scale thermal drawing of PEI films.[11,12,14]

3. Conclusion

In summary, we demonstrated a new interfacial polymerization (IP) route for the synthesis of high-performance PEI films based on the reaction of an organic dianhydride with an aqueous diamine to form PAA, followed by thermal imidization to PEI. We characterized the underlying transport, reaction and precipitation mechanisms governing the process and demonstrated that while reaction kinetics and monomer transports are dictated by the same kinetics as conventional IP reactions, polymer chains precipitate by nucleation-growth-coarsening as opposed to spinodal decomposition. This results in a unique film morphology, composed of a flat nanoscale layer supporting spherical colloids. The PEI films feature optical and thermal properties on par with those of commercial PEI. The number average molecular weight of IP PEI is slightly lower than that of Ultem with a greater PDI, indicating a higher melt index and improved processability. This rapid polymerization reaction shows great potential for scaleup in a continuous process, which has been demonstrated for conventional IP of acid chloride monomers in the context of thin film composite (TFC) membranes and fiber coatings.[57–59]. Adaptation of this work to a continuous manufacturing process could reduce the cost of producing PEI and expand its uses in applications such as thin film capacitors and composite materials.[54]

4. Experimental Section

Materials: Bisphenol A dianhydride (BPADA) (⩾97%) was purchased from Ambeed, Inc. and m-phenylene diamine (MPD) (⩾99%) was obtained from Millipore Sigma. Both were used without further purification and stored without UV light exposure and under nitrogen to prevent any hydrolysis or degradation. Benzene (suitable for HPLC, ⩾99.9%), methyl ethyl ketone (MEK - suitable for HPLC, ⩾99.7%), and water (suitable for HPLC) were all obtained from Millipore Sigma and used without further purification. N,N-dimethylformamide (DMF - HPLC Grade) and lithium bromide (anhydrous) for gel permeation chromatography sample preparation were obtained from Alfa Aesar. All glassware and reaction hardware were thoroughly washed with acetone then scrubbed and washed with water and an Alconox detergent solution. All glassware were then rinsed with deionized water, dried in a laboratory oven at 80 °C, and cooled down to room temperature before use.

IP of PAA and Imidization to PEI: A 100 mL round bottom flask equipped with a stir bar was loaded with the desired mass of BPADA (0.62–1.87 g). 40 mL of benzene-MEK mixture in the desired volume ratio was then added to the flask that was capped and left to stir at 400 rpm in a temperature-controlled water bath at 50 °C until the monomer was fully dissolved (≈5–15 min). In the meantime, a 100 mL beaker equipped with a stir bar was loaded with the desired mass of MPD (0.13–0.39g). 40 mL of water was added and the aqueous MPD solution was left to stir at 400 rpm at room temperature until fully dissolved (≈5 min). Once BPADA was fully dissolved in the organic phase, the flask was withdrawn from the aqueous bath and left to cool in ambient conditions for 15 min. Throughout this study, BPADA and MPD were kept in a one-to-one molar ratio. This means that the molar concentration of MPD in the aqueous solution was always to that of BPADA in the organic solvent, and that the same volume was used for both phases. The IP reaction of organic BPADA and aqueous MPD was conducted in a 200 mL beaker equipped with a custom polymer film collector resting at the bottom of the reaction vessel. A custom procedure for IP of PAA at the organic-aqueous interface was created to ensure polymer film collection repeatably and without damaging its morphology. The overall procedure is detailed in the Supporting Information (Figure S1, Supporting Information) where the synthesis and collection steps are described. A sample collector, constituted of a 316L stainless steel mesh with handles supporting a piece of filter paper, was set to rest at the bottom of the beaker. The mesh and filter paper were the same diameter as the beaker to minimize polymer losses upon film pickup. The aqueous MPD solution (40 mL) was poured into the reaction vessel due to its higher density. The organic BPADA solution (40 mL) was slowly poured on top of the aqueous phase to minimally disrupt the liquid-liquid interface. After a reaction time of 1–10 min, the majority of the top and bottom phases was pipetted out to lower the polymer film to the close proximity of the filter paper. The PAA film was then collected onto the filter paper by lifting up the polymer film collector. The collecting device and polymer films were then slowly plunged into water, benzene and then water again to wash unreacted monomer species without inducing film cracking. The polymer film on its filter paper substrate was then taken off the stainless steel mesh and left to dry in ambient conditions for 2–3 h. The dry PAA film was then recovered by lifting it off the filter paper backing. The dry PAA film was transferred to a disposable aluminum weighing dish and thermally imidized in a Buchi glass oven (B-585) under vacuum according to the following thermal profile: 1 h at 150 °C, 12 h at 180 °C, then 4 h at 200 °C.

Microscopy and Film Morphology Assessment: Polymer film morphology was assessed by Scanning Electron Microscopy (SEM) on a Zeiss Gemini 450 SEM using the in-lens detector, an acceleration voltage of 3 kV, and a probe current of 100 pA. Prior to imaging, polymer film flakes were mounted on SEM studs using carbon tape and coated with 8–10 nm of gold using a benchtop Balzer sputterer. Thin film thickness τ and colloid layer height h_c were observed on cross-sectional areas of the polymer films. An average and standard deviation across 10 regions of tgree samples obtained under the same conditions were used to plot the various characteristic sizes and their error bars. The distribution of colloid diameters under given synthesis conditions was obtained by analyzing top–down SEM views of the colloid-rich surface of the polymer film. Values of d_c were obtained across images at the same magnification, using an automated circle detection algorithm implemented in MATLAB. The contrast was first enhanced using histogram equalization. The grayscale images were then eroded and morphologically reconstructed. The edges in intensity were found for each image, and circular features were found and measured using MATLAB *imfindcircles* function. The areal number concentration of colloids N_p was obtained by dividing the number of measured colloids by the area of the image. An average and standard deviation across five images for three samples obtained under the same conditions were used to plot the evolution of the colloid diameters d_c and N_p and their associated error bars.

Optical Property Characterization: Structural color formation and reflection spectra for the nanostructured PAA and PEI films were evaluated by spectroscopy combined with optical microscopy. All optical measurements were performed on an Olympus BX51 optical microscope equipped with a 20x objective (Olympus UPlanFL) and an Olympus U-ULH Halogen light source (U-ULS100H). Images were acquired with a RGB Allied Vision Technologies Prosilica GT camera mounted on the microscope's imaging port, and with a closed aperture stop (AS). Reflected light was collected via a 40 mm focal length visible achromat lens and an optical fiber (Ø50 µm) with a collection spot size of 12 µm at the sample. The spectra were recorded using an optical spectrometer (Ocean Optics Maya2000 Pro) and Ocean View software. The reference spectrum was obtained from a flat mirror, while background was taken from a light-absorbing sample of black felt. All spectra were measured by focusing the light on the flat side of the polymer film, which forms facing the aqueous phase (the other side is textured with colloid formation). Thin film interference spectra were modelled in a custom MATLAB code based on Rouard approach.[60] The refractive index and film thickness were adjusted to match the experimentally measured spectra of the PAA and PEI thin films. Each spectrum was then plotted in the CIE x-y color space, using the International Commission on Illumination (CIE 1931) 1931 2° Standard Observer color matching functions, implemented in MATLAB.[61] The process involved integrating the reflectivity spectra with three standard "matching functions", which account for the response of the three different photoreceptors in the eye. An average and standard deviation across the refractive index and the thickness fit for three different films obtained under the same conditions were used for graphical representation.

Thermal Property Assessment: The thermal stability of PAA and PEI was evaluated through thermogravimetric analysis (TGA) performed on a TA instrument Discovery TGA 550. Approximately 1–5 mg of powdered polymer samples was loaded into a Platinum HT pan. The temperature was increased from 40 °C to 800 °C at a heating rate of 10 °C min^{-1} in Nitrogen. Differential Scanning Calorimetry (DSC) was used to measure the glass transition temperature of the obtained PEI nanostructured films. About 6 mg of PAA was loaded in a T-zero pan, crimped with a T-zero hermetic lid (TA Instrument). A hole was pierced in the lid with an 18G needle to let water escape and the samples were imidized in the conditions described above. Imidization in the T-zero pan minimizes polymer loss upon transferring from the imidization dish to the DSC pan. DSC was conducted on a TA instrument Discovery DSC 250 equipped with an RCS cooler at a heating rate of 20 °C min^{-1} in Nitrogen, from 25 °C to 275 °C. Both TGA and DSC data were then analyzed using TA instrument software TRIOS.

Fourier Transform Infrared (FT-IR) Spectroscopy: FT-IR spectra were acquired using a Bruker ALPHA II FT-IR spectrometer equipped with the platinum Attenuated Total Reflection (ATR) accessory (diamond crystal). Thirty-two (32) scans were used for each acquisition and the raw signals were corrected by removing the baseline and atmospheric contributions using Bruker OPUS spectroscopy software.

Measurement of PEI Molecular Weight Distribution: PEI samples (1–3 mg) were dissolved into 1 mL of DMF with 0.025 mol L^{-1} LiBr and placed on a shaker table for 16 h to dissolve before filtering through 0.2 µm PTFE filters. Gel Permeation Chromatography (GPC)

measurements were conducted on an Agilent 1260 II detector suite and Agilent PolyPore Column at 60 °C using DMF with 0.025 mol L^{-1} LiBr as the eluent, 50 µm injection volumes, and a flow rate of 1.0 mL min^{-1}. Concentration was tracked using a UV detector at 275 nm and molar masses were calculated as a function of a monodisperse polystyrene calibration standard. An average and standard deviation across three different samples obtained under the same conditions were used to plot the number average molecular weight evolution with synthesis parameters and the associated error bars.

PEI thin Film Capacitor Measurements: Prototype capacitors were fabricated from a PEI film sandwiched between two aluminum blocks, milled flat with an overlapping area of 7 mm × 7 mm. Silver conductive paste was applied to both aluminum electrodes before establishing contact with the PEI film. Capacitance measurements were taken with the Hioki IM3536 LCR meter at 100 kHz; further tests at 10 kHz and 1 MHz showed little to no change in the measurements. Average values and standard deviations were obtained by measuring the capacitance of three regions of the same PEI film. Estimated capacitances were calculated by using the ideal parallel plate capacitor model, using porosities estimated from SEM images. The porosities were estimated using Python and OpenCV by cropping the region of interest, applying a binary filter, and comparing the number of black and white pixels. Average and standard deviation of film porosity were obtained by analyzing three SEM images of the same PEI film.

CNT-PEI Composite Fabrication: Details on the CNT sheets used for composite fabrication and in-situ interfacial polymerization (ISIP) process can be found elsewhere.[54,55] ISIP was conducted using BPADA as the organic monomer, with $\phi_{Bz} = 0.5$, $[MPD]_0 = [BPADA]_0 = 0.07$ mol L^{-1}, and $t_{rxn} = 5$ min.

Supporting Information

Supporting Information is available from the Wiley Online Library or from the author.

Acknowledgements

The authors thank Prof. Zachary, P. Smith, and Dr. Justin Teesdale for access to thermogravimetric analysis tools and associated support, and Prof. Mathias Kolle and Benjamin A. Miller for providing access to optical characterization tools and for useful discussions. The authors also thank William J. Sawyer for insightful discussions regarding this work, and Dr. Joseph D. Sandt for support in developing the thin-film interference optical model, and Dr. Margaret Lee for preliminary gel permeation chromatography measurements. This work made use of the electron microscopy facilities at MIT.nano, and thermal characterization equipment at MIT's Institute of Soldier Nanotechnologies (ISN). Funding was provided by the NASA Space Technology Research Institute (STRI) for Ultra-Strong Composites by Computational Design (US-COMP, Grant ID NNX17AJ32G), the National Science Foundation (CMMI-2114343), and the MIT Professor Amar G. Bose Research Grant Program. Dr. Chazot was also supported by a MathWorks Engineering Fellowship at MIT for academic years 2020–2021 and 2021–2022.

Conflict of Interest

The authors declare no conflict of interest.

Data Availability Statement

The data that support the findings of this study are available from the corresponding author upon reasonable request.

Keywords

colloids, interfacial polymerizations, nucleation, polyetherimide, polymers, thermoplastics, thin films

Received: December 13, 2022
Revised: February 6, 2023
Published online: March 6, 2023

[1] D. M. White, T. Takekoshi, F. J. Williams, H. M. Relles, P. E. Donahue, H. J. Klopfer, G. R. Loucks, J. S. Manello, R. O. Matthews, R. W. Schluenz, *J. Polym. Sci., Polym. Chem. Ed.* **1981**, *19*, 1635.
[2] R. O. Johnson, H. S. Burlhis, *J. Polym. Sci., Polym. Symp.* **1983**, *70*, 129.
[3] S. Carroccio, C. Puglisi, G. Montaudo, *Macromol. Chem. Phys.* **1999**, *200*, 2345.
[4] E. R. Long Jr, W. D. Collins, *Polym. Eng. Sci.* **1988**, *28*, 823.
[5] Y. Alqaheem, A. Alomair, *J. Chin. Chem. Soc.* **2019**, *66*, 1738.
[6] R. Naim, A. F. Ismail, T. Matsuura, I. A. Rudaini, S. Abdullah, *RSC Adv.* **2018**, *8*, 3556.
[7] H. Zhang, H. Mao, J. Wang, R. Ding, Z. Du, J. Liu, S. Cao, *J. Membr. Sci.* **2014**, *470*, 70.
[8] X. Wu, G. Zhou, X. Cui, Y. Li, J. Wang, X. Cao, P. Zhang, *ACS Appl. Mater. Interfaces* **2019**, *11*, 17804.
[9] A. Ghosh, S. K. Sen, S. Banerjee, B. Voit, *RSC Adv.* **2012**, *2*, 5900.
[10] G. C. Eastmond, J. Paprotny, R. S. Irwin, *Macromolecules* **1996**, *29*, 1382.
[11] D. Q. Tan, *Adv. Funct. Mater.* **2020**, *30*, 1808567.
[12] D. Q. Tan, X. Wu, *Mater. Today Energy* **2022**, *30*, 101167.
[13] Pei dielectric film for evs performs at 150°C, **2021**, https://www.plasticstoday.com/automotive-and-mobility/pei-dielectric-film-evs-performs-150%C2%B0c.
[14] D. Tan, L. Zhang, Q. Chen, P. Irwin, *J. Electron. Mater.* **2014**, *43*, 4569.
[15] D. Guo, A. U. Khan, T. Liu, Z. Zhou, G. Liu, *Polym. Chem.* **2019**, *10*, 379.
[16] J. Kurdi, A. Tremblay, *Polymer* **2003**, *44*, 4533.
[17] L. Hao, P. Li, T.-S. Chung, *J. Membr. Sci.* **2014**, *453*, 614.
[18] J. Wang, T. R. Pozegic, Z. Xu, R. Nigmatullin, R. L. Harniman, S. J. Eichhorn, *Compos. Sci. Technol.* **2019**, *182*, 107744.
[19] D. M. Sato, L. M. Guerrini, M. P. de Oliveira, L. R. de Oliveira Hein, E. C. Botelho, *Mater. Res. Express* **2018**, *5*, 115302.
[20] B.-K. Chen, Y.-T. Fang, J.-R. Cheng, *Macromol. Symp.* **2006**, *242*, 34.
[21] X. Chen, T. Yang, Q. Zhang, L. Chen, V. Bobnar, C. Rahn, Q. Zhang, *Nano Energy* **2021**, *88*, 106225.
[22] J. Hutfles, W. Chapman, J. Pellegrino, *J. Appl. Polym. Sci.* **2018**, *135*, 45993.
[23] J.-J. Shieh, T.-S. Chung, *Ind. Eng. Chem. Res.* **1999**, *38*, 2650.
[24] Cost were estimated by searching both materials in 25 kg quantities on http://www.alibaba.com, excluding shipping cost.
[25] P. Morgan, S. Kwolek, *J. Polym. Sci.* **1958**, *40*, 299.
[26] N. Gao, J. Yu, S. Chen, X. Xin, L. Zang, *Synth. Met.* **2021**, *273*, 116693.
[27] C. Feng, K. C. Khulbe, T. Matsuura, *J. Appl. Polym. Sci.* **2010**, *115*, 756.
[28] Z. Tan, S. Chen, X. Peng, L. Zhang, C. Gao, *Science* **2018**, *360*, 518.
[29] E. Quevedo, J. Steinbacher, D. T. McQuade, *J. Am. Chem. Soc.* **2005**, *127*, 10498.
[30] X. Lu, M. Elimelech, *Chem. Soc. Rev.* **2021**, *50*, 6290.
[31] C. Hansen, *Hansen Solubility Parameters: A User's Handbook*, 2nd Ed., CRC Press, Boca Raton, **2007**.

[32] D. Van Krevelen, K. Te Nijenhuis, *Properties of Polymers*, Elservier, Amsterdam, ISBN 9780080548197, **2009**, pp. 189–227.
[33] P. J. Flory, *Principles of Polymer Chemistry*, Cornell University Press, Ithaca, **1953**.
[34] R. W. Balluffi, S. M. Allen, W. C. Carter, *Kinetics of Materials*, Wiley, New York, **2005**.
[35] C. V. Thompson, *Annu. Rev. Mater. Sci.* **2000**, *30*, 159.
[36] S. K. Karode, S. S. Kulkarni, A. K. Suresh, R. A. Mashelkar, *Chem. Eng. Sci.* **1997**, *52*, 3243.
[37] S. K. Karode, S. S. Kulkarni, A. K. Suresh, R. A. Mashelkar, *Chem. Eng. Sci.* **1998**, *53*, 2649.
[38] R. Li, Z. Chen, J. Li, C. Zhang, Q. Guo, *Synth. Met.* **2013**, *171*, 39.
[39] F. W. Harris, *Synthesis of Aromatic Polyimides from Dianhydrides and Diamines*, Springer, Netherlands, Dordrecht, ISBN 978-94-010-9661-4, **1990**, pp. 1–37.
[40] J. Robertson, T. Centeno-Hall, A. Padias, R. Bates, H. Hall, *Polymers* **2012**, *4*, 741.
[41] S. Twomey, *Geofis. Pura Appl.* **1959**, *43*, 243.
[42] J.-M. Cohard, J.-P. Pinty, C. Bedos, *J. Atmos. Sci.* **1998**, *55*, 3348.
[43] H. F. Mark, S. M. Atlas, N. Ogata, *J. Polym. Sci.* **1962**, *61*, 49.
[44] E. D. Johnson, Ph.D. Thesis, Carnegie Mellon University, **1985**.
[45] A. Nowbahar, V. Mansard, J. M. Mecca, M. Paul, T. Arrowood, T. M. Squires, *J. Am. Chem. Soc.* **2018**, *140*, 3173.
[46] Sabic innovative plastics ultem resin characteristics, can be found under https://www.sabic.com/en/products/specialties/ultem-resins/ultem-resin, **2022**.
[47] P. Hiemenz, T. Lodge, *Polymer Chemistry - Third Edition*, CRC Press, Boca Raton, **2020**.
[48] G.-J. W. Jan Paul Penning, R. Puyenbroek, High performance thermoplastic compositions with improved melt flow behavior, **2002**, US Patent No. 6,417,255 B1.
[49] O. Olabisi, K. Adewale, *Handbook of Thermoplastics*, CRC Press, Boca Raton, **2016**.
[50] S. Morino, K. Horie, *Polym. J.* **1999**, *31*, 707.
[51] R. L. Mercado, Y. Wang, T. D. Flaim, W. L. DiMenna, U. Senapati, In J. G. Grote, T. Kaino, editors, *Organic Photonic Materials and Devices VI*, vol. *5351*, International Society for Optics and Photonics, SPIE, **2004**, pp. 276–283.
[52] J. Seo, W. Jang, H. Han, *J. Appl. Polym. Sci.* **2009**, *113*, 777.
[53] Sabic - an introduction to ultem thin film, **2019**, https://www.sabic.com/en/products/documents/an-introduction-to-ultem-thin-film/en.
[54] C. A. C. Chazot, C. K. Jons, A. J. Hart, *Adv. Funct. Mater.* **2020**, *30*, 2005499.
[55] C. A. C. Chazot, B. Damirchi, B. Lee, A. C. T. van Duin, A. J. Hart, *Nano Lett.* **2022**, *22*, 998.
[56] Y.-D. Lee, H.-B. Tsai, J.-T. Jeng, *J. Polym. Sci., Polym. Chem.* **1988**, *26*, 2039.
[57] D. B. L. C. Scala, D. F. Ciliberti, Interface condensation desalination membranes, **1973**, US Patent 3,744,642.
[58] H. O. A. Kumano, T. Hayashi, Composite hollow fiber membrane and process for its production, **1998**, US Patent No. 5,783,079.
[59] R. Whitfield, L. Miller, W. Wasley, *Text. Res. J.* **1961**, *31*, 704.
[60] O. S. Heavens, *Optical Properties of Thin Solid Films*, Dover Publications, New York, **1965**.
[61] J. D. Sandt, M. Moudio, J. K. Clark, J. Hardin, C. Argenti, M. Carty, J. A. Lewis, M. Kolle, *Adv. Healthcare Mater.* **2018**, *7*, 1800293.